

# GMC COLLISIONS AS TRIGGERS OF STAR FORMATION. V. OBSERVATIONAL SIGNATURES

THOMAS G. BISBAS<sup>1,2</sup>, KEI E. I. TANAKA<sup>1</sup>, JONATHAN C. TAN<sup>1,3,4</sup>, BENJAMIN WU<sup>4</sup>, AND FUMITAKA NAKAMURA<sup>4</sup>

*Draft version December 14, 2024*

## ABSTRACT

We present calculations of molecular, atomic and ionic line emission from simulations of giant molecular cloud (GMC) collisions. We post-process snapshots of the magneto-hydrodynamical simulations presented in an earlier paper in this series by Wu et al. (2017a) of colliding and non-colliding GMCs. Using photodissociation region chemistry and radiative transfer we calculate the level populations and emission properties of  $^{12}\text{CO}$   $J = 1 - 0$ , [C $\text{I}$ ] (1-0) at 609  $\mu\text{m}$ , [C $\text{II}$ ] 158  $\mu\text{m}$  and [O $\text{I}$ ]  $^3\text{P}_1 \rightarrow ^3\text{P}_0$  transition at 63  $\mu\text{m}$ . From integrated intensity emission maps and position-velocity diagrams, we find that the fine-structure lines and in particular the [C $\text{II}$ ] 158  $\mu\text{m}$  can be used as a diagnostic tracer for cloud-cloud collision activity. Our results hold even in already evolved systems whose collision signature in molecular lines has been diminished.

**Keywords:** ISM: clouds — ISM: kinematics and dynamics — ISM: lines and bands — ISM: magnetic fields — ISM: structure — methods: numerical

## 1. INTRODUCTION

Giant Molecular Cloud (GMC) collisions are a potential mechanism for triggering star formation activity in such clouds (e.g. Scoville et al. 1986; Higuchi et al. 2010; Duarte-Cabral et al. 2010; Fukui et al. 2014; Balfour et al. 2015; Torii et al. 2017). Models of galactic shear-driven collisions (Gammie et al. 1991; Tan 2000; Tasker & Tan 2009; Dobbs et al. 2015) may help explain global galactic star formation relations (Tan 2010; Suwannajak et al. 2014). GMC collisions may also be an important mechanism for driving turbulence within GMCs (Tan et al. 2013; Jin et al. 2017; Li et al. 2017). Thus it is important to develop theoretical and numerical models for such collisions and then use them to calculate the observational signatures of these events (e.g., Duarte-Cabral et al. 2011; Inoue & Fukui 2013; Takahira et al. 2014; Haworth et al. 2015a,b).

With the above goal in mind, this paper continues the work of Wu et al. (2015, 2017a) (Papers I and II) in studying GMC collisions via ideal magneto-hydrodynamic (MHD) simulations. In particular, Paper II studied the kinematics and dynamics of collisions of turbulent, magnetized, multiphase (via photodissociation region (PDR)-based heating/cooling functions) GMCs using synthetic observations in the optically thin limit. Here, we provide a more realistic treatment of the radiative transfer of line emission from multiple species from these simulations with a tool we develop that accounts for velocity-dependent optical depth along the line-of-sight. Other papers in this series have added additional physics: Wu et al. (2017b) (Paper III) included star formation via various sub-grid models, including simulations in which star formation depends on the local mass to magnetic flux ratio; Christie et al. (2017) (Paper IV) studied the effects of ambipolar diffusion, especially its effects on the efficiency of dense core formation. However, here, with our focus on observational signatures, we

return to the simulation outputs of Paper II for our analysis. We note that these simulations do not include star formation or any localized feedback, so the results we present will isolate the “pure” signature of the GMC-GMC collision process, separate from these complicating factors.

Our paper is organized as follows. In §2 we give a brief outline of the snapshots we selected of the MHD simulations performed in Paper II (§2.1), of the photo-dissociation region calculations (§2.2) and of the radiative transfer tool we develop (§2.3). In §3 we discuss the signatures frequently used by the observational community to identify cloud-cloud collision activity. In §4 we report our results, which are then further discussed in §5. We conclude in §6.

## 2. NUMERICAL METHODS

### 2.1. Magneto-hydrodynamical simulations

For the purposes of this work we use two snapshots from the three-dimensional MHD simulations performed in Paper II. These simulations include self-gravity, supersonic turbulence and magnetic fields (treated in the limit of ideal MHD). They have been performed with the adaptive-mesh refinement (AMR) code ENZO (Bryan et al. 2014). The two GMCs considered are initially spherical and uniform with total H-nucleus number density of  $n_{\text{H}} = 100 \text{ cm}^{-3}$ , radius of  $R = 20 \text{ pc}$  and thus with mass of  $M = 9.3 \times 10^4 M_{\odot}$ . The ambient medium consists of gas with  $n_{\text{H}} = 10 \text{ cm}^{-3}$ . The spatial resolution of the AMR grid has a minimum value of 0.125 pc. A magnetic field with strength  $B = 10 \mu\text{G}$  has been included, directed at an angle of  $\theta = 60^\circ$  with respect to  $x$ -direction. The centers of GMCs have an initial separation of  $2R$  in the  $x$ -direction and 0 in the  $z$ -direction. Along the  $y$ -direction they are offset by an impact parameter  $b = 0.5R$ . Both GMCs have a one-dimensional turbulent velocity dispersion of  $\sigma_v = 5.2 \text{ km s}^{-1}$ .

As described in Paper I, the simulations include PDR-based heating and cooling processes to determine gas and dust temperature and the emission properties from various species. An isotropic FUV radiation field with strength  $G/G_0 = 4$  (i.e., 4 times the Habing 1968, estimate of the local FUV intensity) and a cosmic-ray ionization rate of  $\zeta_{\text{CR}} = 10^{-16} \text{ s}^{-1}$  have been considered. These values represent conditions observed in the inner part of the Galaxy at distances of  $\sim 4 \text{ kpc}$  from

Electronic address: TGB: tgbas@ufl.edu

<sup>1</sup> Department of Astronomy, University of Florida, Gainesville, FL 32611, USA

<sup>2</sup> Max-Planck-Institut für Extraterrestrische Physik, Giessenbachstrasse 1, D-85748 Garching, Germany

<sup>3</sup> Department of Physics, University of Florida, Gainesville, FL 32611, USA

<sup>4</sup> National Astronomical Observatory of Japan, Mitaka, Tokyo, 181-8588, Japan

the Galactic Centre. Further details are discussed in Papers I and II.

We select two different cases from the above set of simulations: i) the case where the clouds collide at a relative speed of  $v_{\text{rel}} = 10 \text{ km s}^{-1}$  (“colliding”) in which they are moving at equal but opposite velocities along the axis of collision (i.e.  $+v_{\text{rel}}/2 = +5 \text{ km s}^{-1}$  and  $-v_{\text{rel}}/2 = -5 \text{ km s}^{-1}$ ), and ii) the case where the clouds do not collide (“non-colliding”) but overlap each other along the line-of-sight, therefore the relative speed is  $v_{\text{rel}} = 0 \text{ km s}^{-1}$ . The selected snapshots for the colliding case are at times of  $t = 2$  and  $4 \text{ Myr}$  and are shown in the top and middle rows of Fig. 1. The collision occurs along the  $x$ -direction. For the non-colliding case, we consider only the snapshot at  $t = 4 \text{ Myr}$  which is shown at the bottom row of Fig. 1.

### 2.2. 3D-PDR calculations

To perform realistic radiative transfer calculations (see §2.3) and obtain the emission map of a particular line, we need knowledge of the corresponding level populations, abundances of species, as well as gas and dust temperature profiles. To do this, we use the 3D-PDR code<sup>5</sup> (Bisbas et al. 2012), which treats the chemistry of PDRs using various cooling and heating processes. Although the code is able to calculate three-dimensional PDRs of arbitrary density distributions, the computational cost for post-processing the above hydrodynamical snapshots at the given resolution is prohibitively high. Instead, we perform an extended one-dimensional grid of uniform density slabs irradiated by a plane-parallel radiation field and we adopt the methodology described in Paper I, which connects the H-nucleus number density  $n_{\text{H}}$  of a cell with a most probable visual extinction value,  $A_V$ .

The density range spanning the grid of one-dimensional simulations is  $1 \text{ cm}^{-3} < n_{\text{H}} < 10^7 \text{ cm}^{-3}$  at a precision of 0.1 dex. This resolution gives a set of a total of 70 simulations. In all these calculations we considered a plane-parallel radiation field with strength  $\chi/\chi_0 = 4$  and a cosmic-ray ionization rate of  $\zeta_{\text{CR}} = 10^{-16} \text{ s}^{-1}$ , thus mimicking the conditions adopted in Papers I and II. We considered a reduced UMIST 2012 chemical network (McElroy et al. 2013) of 33 species and 330 reactions and we adopted the “standard” ISM abundances of elements, i.e.,  $[\text{He}]/[\text{H}] = 0.1$ ,  $[\text{C}]/[\text{H}] = 10^{-4}$ , and  $[\text{O}]/[\text{H}] = 3 \times 10^{-4}$ .

### 2.3. Radiative Transfer calculations

We construct a radiative transfer tool described in Appendix A which we use for our synthetic observations. As mentioned in §2.1, the MHD simulations use an AMR grid, effectively meaning that the spatial resolution is higher in places of higher density. For the radiative transfer calculations, however, we convert the selected snapshots to an uniform grid of  $0.125 \text{ pc}$  resolution. This in turn gives a grid consisting of  $512^3$  cells which we use to solve for the radiative transfer along each line-of-sight.

Once the radiative transfer equation is solved (see Appendix A), we calculate the antenna temperature,  $T_{\text{A}}$ , using the following relation and assuming that the main beam efficiency of a hypothetical telescope is unity:

$$T_{\text{A}} = \frac{c^2 I_{\nu}}{2k_{\text{B}}\nu^2}. \quad (1)$$

<sup>5</sup> <https://uclchem.github.io/3dpdr.html>

Here,  $c$  is the speed of light,  $k_{\text{B}}$  is the Boltzmann constant, and  $I_{\nu}$  is the intensity over frequency  $\nu$ , defined as

$$\nu = \nu_0 \left( 1 - \frac{v_{\text{los}}}{c} \right), \quad (2)$$

where  $\nu_0$  denotes the frequency in the observer reference frame and  $v_{\text{los}}$  is the velocity along the line-of-sight. The integrated antenna temperature over velocity,  $W$ , can be evaluated using the following relation:

$$W = \frac{c^3}{2k_{\text{B}}\nu_0^3} \int_{\nu_0 - \Delta\nu/2}^{\nu_0 + \Delta\nu/2} I_{\nu} d\nu, \quad (3)$$

where  $\Delta\nu$  is the bandwidth of the integration. To construct the emission maps, the velocity width we assume is  $-15 \text{ km s}^{-1} < v_{\text{los}} < +15 \text{ km s}^{-1}$ .

Unless stated, the radiative transfer algorithm has been applied along the  $x$ -direction, which is the axis of collision. The chosen direction of integration is from  $+x$  to  $-x$ . With the collision occurring along the line-of-sight, we expect to see the most clear signature of its effect. We do this in order to see how such signatures in different lines vary and how fine-structure lines compare with the commonly used low- $J$  CO lines and particularly with CO  $J = 1 - 0$ . We will also examine how the GMCs appear when viewed from a direction perpendicular to the collision axis, which is the other extreme, i.e., for which the signatures of the collision would be minimized.

### 3. THE “BRIDGE-EFFECT” SIGNATURE

An observational technique to identify a collision event between two clouds is to construct their position-velocity (p-v) diagram and look for a double velocity peak along the line-of-sight. The peaks should not be in the form of two isolated “islands” in the p-v diagram, but they should be linked via a “bridge”. This indicates the presence of a pair of clouds along the line-of-sight that are connected with a region where the velocity transitions between the two main values of each cloud, implying a mutual interaction. Such double velocity peaks have been observed in various objects. For example, C<sup>18</sup>O  $J = 1 - 0$  observations in the Serpens star-forming region by Duarte-Cabral et al. (2010) confirm the existence of a double-peak in the p-v diagram. The corresponding velocity width has been estimated as  $\sim 2 \text{ km s}^{-1}$ . They explain this feature using Smoothed particle hydrodynamics (SPH) simulations of two colliding cylinders (Duarte-Cabral et al. 2011) in which the resulting p-v diagram is reminiscent to the one observed in the Serpens region. Torii et al. (2011) provide p-v diagrams of the Trifid Nebula (M20) in which a broad bridge effect connecting multiple velocity peaks along the line-of-sight is observed. Similarly, Nakamura et al. (2012) presented high spatial resolution images of the <sup>12</sup>CO  $J = 1 - 0$  line for a wide region including the L1641-N cluster. They find two-velocity component gas along the line-of-sight suggesting a cloud-cloud collision event. The velocity width is  $\sim 3 \text{ km s}^{-1}$  which is about three times higher than the local turbulent velocity ( $v_{\text{turb}} \sim 1 \text{ km s}^{-1}$ ). Recently, Fukui et al. (2017a) identified double velocity peaks in the <sup>12</sup>CO  $J = 1 - 0$  line of the molecular gas toward M42 and M43 which potentially implies that the northern part of the Orion A cloud may have been formed by two colliding clouds.

Using hydrodynamical simulations, Haworth et al. (2015a,b) discuss extensively how the bridge effect occurs and develops in p-v diagrams of the <sup>12</sup>CO  $J = 1 - 0$  line.

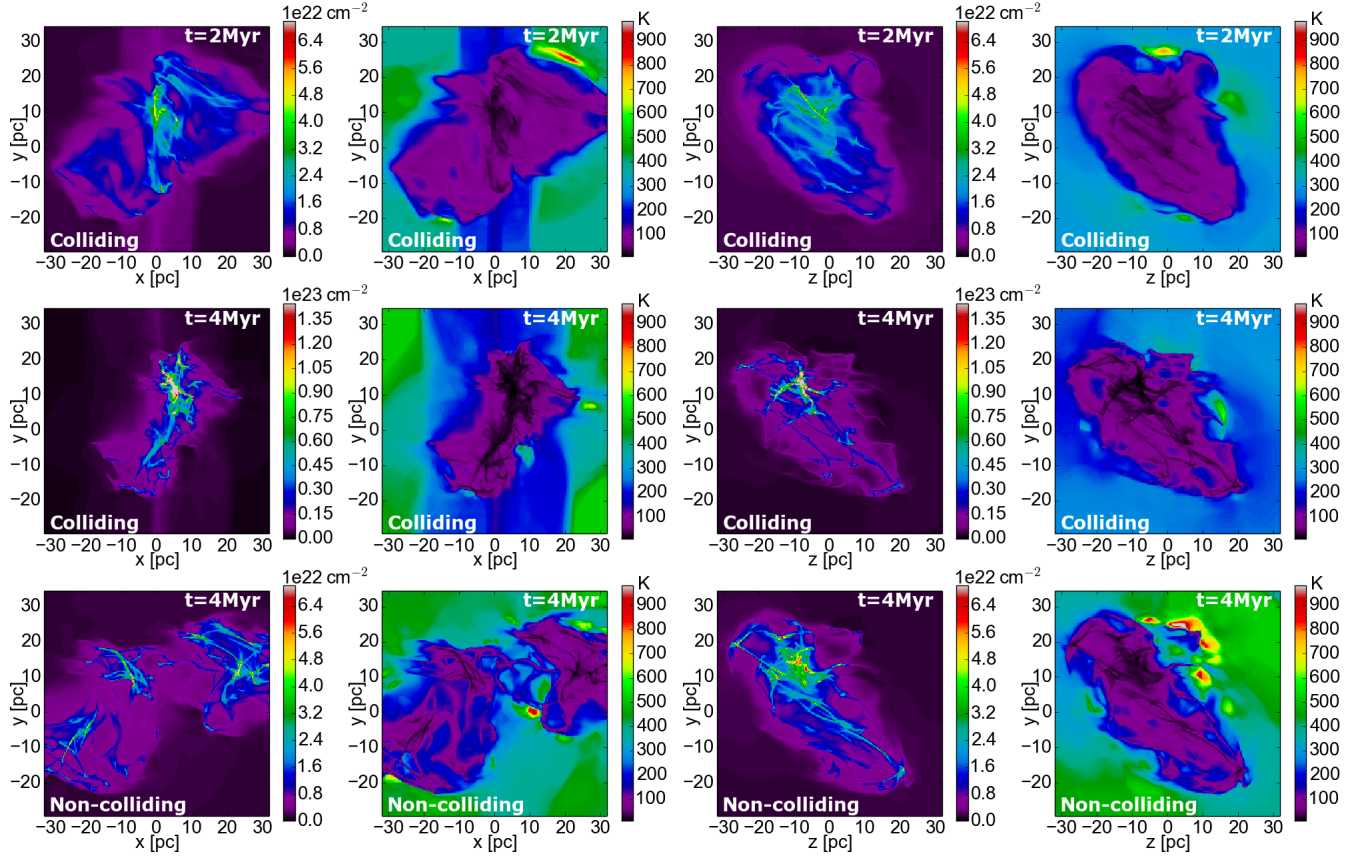


**Figure 1.** Maps of the total H-nucleus column density (first and third columns) and mass-weighted gas temperature (second and fourth columns) of the MHD simulations from Paper II. The integration in the maps of the first two columns is along the  $z$ -direction, whereas in the third and fourth columns it is along the  $x$ -direction, i.e., the direction along which the collision occurs. The first and the second rows show snapshots at  $t = 2$  and  $4$  Myr of the “colliding” case. The bottom row corresponds to the  $t = 4$  Myr snapshot for the “non-colliding” case.

They examine various cases and at different viewing angles of colliding and non-colliding cases and they additionally examine p-v diagrams of isolated clouds including radiative feedback (HII regions). They find that the bridge feature holds for a small fraction of the  $4\pi$  sr (e.g., about 20-30% for a  $v_{\text{rel}} = 10 \text{ km s}^{-1}$  head-on collision, which is the collision velocity considered here). Furthermore, they find that this signature is resilient to radiative feedback from stars formed in the simulations and cannot be easily reproduced by kinematical behaviour other than a cloud-cloud collision. A double velocity peak or bridge (“bridge-effect”) can therefore act as a signature of an undergoing collision event.

#### 4. RESULTS

We construct integrated intensity emission maps and position-velocity (p-v) diagrams for all four snapshots we considered. The particular p-v diagrams are calculated by averaging over the entire  $y$ -direction at each different velocity,  $v$ , as a function of the  $z$ -direction. To highlight the bulk motions that are a signature of a cloud collision, we also show maps of integrated intensity of only higher velocities, i.e.,  $> +5 \text{ km s}^{-1}$  (redshifted) and  $< -5 \text{ km s}^{-1}$  (blueshifted). This emission will mostly correspond to gas that moves at velocities greater than those reached due to internal turbulence. We consider four different lines:  $^{12}\text{CO } J = 1 - 0$  (hereafter CO  $J = 1 - 0$ ); [C I]  $1 \rightarrow 0$  (609  $\mu\text{m}$ ); [C II] 158  $\mu\text{m}$ ; and [O I]  $^3\text{P}_1 \rightarrow ^3\text{P}_0$  63  $\mu\text{m}$ .

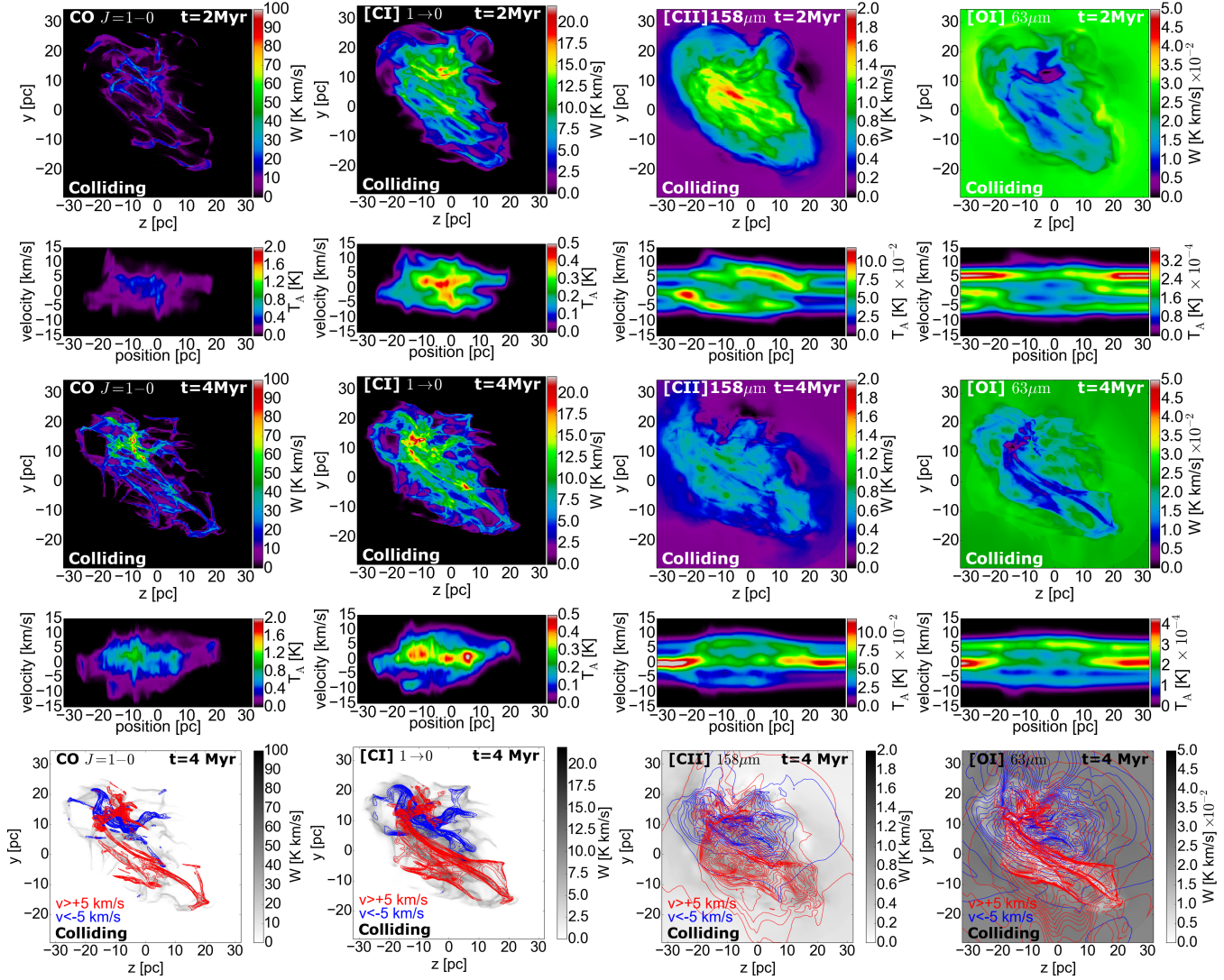
##### 4.1. Colliding case

Figure 2 shows the emission maps (integrated intensity,  $W$ ) and the corresponding p-v diagrams for the colliding case at  $t = 2$  and  $4$  Myr for all different lines considered. The bottom row shows the high velocity gas emission for each case, which we discuss further below. As it can be seen, each different species reveals different parts of the clouds.

The CO  $J = 1 - 0$  transition, which has the strongest emission, originates from the densest parts of the GMCs. Since the collision occurs along the line-of-sight and the density increases as time progresses, at  $t = 4$  Myr the intensity of this CO transition is enhanced compared to that at  $2$  Myr. The enhancement is more prominent in the particular region located at  $z \sim -10 \text{ pc}$  and  $y \sim +10 \text{ pc}$ , where the collision mainly occurs. Here, the total H-nucleus column density reaches a value of  $\gtrsim 2 \times 10^{23} \text{ cm}^{-2}$ . The enhancement in this line is partly because the higher density of the colliding region rapidly extinguishes the FUV radiation.

The [C I] (1-0) line is primarily emitted from the more diffuse gas of both GMCs and hence it reveals the majority of the molecular gas of the clouds (Papadopoulos et al. 2004; Offner et al. 2014; Bisbas et al. 2015, 2017; Glover & Clark 2016). Note that its intensity remains approximately constant as time increases from  $t = 2$  to  $t = 4$  Myr.

The fine-structure line of [C II] 158  $\mu\text{m}$  is emitted from the outer parts of both clouds since they interact with the isotropic FUV radiation field. This line is additionally emitted from the surrounding ambient medium, i.e., the ISM gas in which both GMCs are embedded. Since the density increases due to the collision event, the [C II] emission is decreased at  $t = 4$  Myr



**Figure 2.** Emission maps (first and third rows) and position-velocity diagrams (second and fourth rows) for the colliding case at  $t = 2$  Myr and 4 Myr, respectively. The collision occurs along the line-of-sight. Columns from left to right: CO  $J = 1 - 0$ ; [C I] (1-0); [C II]  $158 \mu\text{m}$ ; O I  $63 \mu\text{m}$ . The bottom row shows the integrated intensity of high velocity gas traced by each line at  $t = 4$  Myr, i.e., maps the gas that has velocities  $> +5 \text{ km s}^{-1}$  (red contours) and  $< -5 \text{ km s}^{-1}$  (blue contours). The contours correspond to the intensity of the line. The grayscale shows the total intensity,  $W$ , of each line. In the p-v diagrams and at  $t = 2$  Myr, the “bridge effect” is better seen in the fine-structure lines of [C II], [O I] and partially in the [C I] line, as all these are primarily emitted from the lower density gas that has not yet undergone collision. Since CO  $J = 1 - 0$  is emitted from the innermost part of both clouds where UV radiation has been severely extinguished, identifying the collision signature in this line once the clouds start to merge is more difficult. Once the collision further evolves ( $t = 4$  Myr), the “bridge-effect” is also diminished for the [C I] (1-0), although still holding in [C II]  $158 \mu\text{m}$  and O I  $63 \mu\text{m}$  lines. The maps of high velocity gas on the other hand show a collision event at  $z \sim -10$  pc and  $y \sim +10$  pc in CO  $J = 1 - 0$  and [C I] (1-0), with the rest of the fine-structure lines indicating the bulk movement of GMCs at a larger scale.

as this line is primarily emitted by lower densities.

Similarly to [C II]  $158 \mu\text{m}$ , the [O I]  $63 \mu\text{m}$  line, although much weaker than all the above lines, originates from the outermost parts of both clouds with significant contributions from the ambient medium of our model. Its overall intensity remains approximately the same between  $t = 2$  and 4 Myr. The  $63 \mu\text{m}$  line is optically thick and due to this, its intensity is remarkably reduced at the parts of the map which correspond to high column densities (see Fig. 1). As it can be seen, the blue-shifted component in the p-v diagrams (i.e., for  $v_{\text{los}} \sim -5 \text{ km s}^{-1}$ ) has a reduced antenna temperature compared to the red-shifted component. We further note that the [O I] line and in particular its ratio with [C I] (1-0) can be used as diagnostic of the intensity of the FUV radiation in PDRs (see Bisbas et al. 2014).

The p-v diagrams in all cases span a width in velocity space

$\sim \pm 10 \text{ km s}^{-1}$ , i.e., resulting from the relative motion of both clouds, that is larger than that due to internal turbulence within the initial GMCs, i.e.,  $\sim \pm 5 \text{ km s}^{-1}$ . As we described above, once the collision process begins,  $W_{\text{CO}(1-0)}$  becomes enhanced. The motion of the gas then becomes more turbulent due to the collision as the two GMCs merge. This is reflected in the p-v diagram at  $t = 4$  Myr in which the overall width in velocity space has increased. As a result, the double velocity peak feature that could indicate collision is diminished (see also Haworth et al. 2015b), although at the position  $\sim -10$  pc (where the collision occurs) the intensity is quite strong over most of the velocity width of  $\sim 20 \text{ km s}^{-1}$ . The p-v diagram of the [C I] (1-0) line at  $t = 2$  Myr indicates, however, that such a feature is reminiscent of the “bridge-effect” discussed in §3 and in particular at position  $\sim 0$  pc. As time progresses and the clouds merge ( $t = 4$  Myr), this signature disappears.



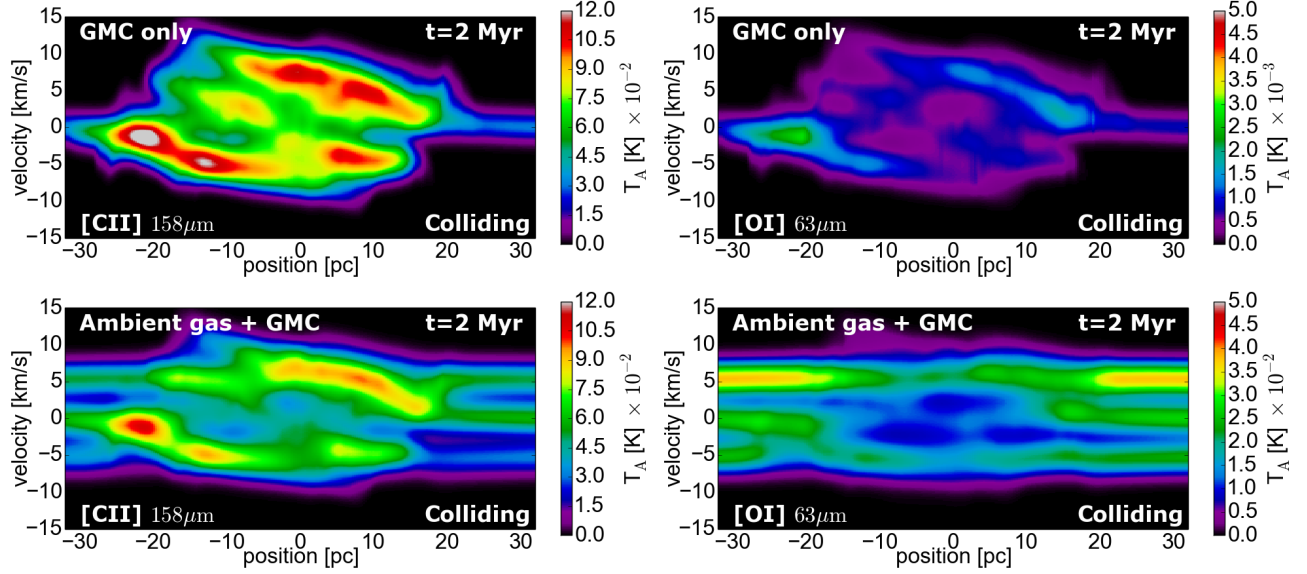


**Figure 3.** Position-velocity diagrams of [CII]  $158\mu\text{m}$  (left column) and [OI]  $63\mu\text{m}$  (right column) for the colliding case at  $t = 2\text{ Myr}$ . In the top row we have deducted the contribution of the ambient ISM gas in the p-v diagram whereas in the bottom row we include the entire domain. The “bridge-effect” is seen in both cases in the [CII] line. In the [OI]  $63\mu\text{m}$  line, it can be seen more clearly in the top p-v diagram considering the GMCs only. Note that the antenna temperature here is 10 times weaker than in the lower panel; the contribution of the ambient ISM gas in the  $63\mu\text{m}$  line in our models obscures the double velocity peak that originates from both GMCs.

For systems whose collision is evolved to the point of erasing or diminishing any potential “bridge-effect” feature in the low- $J$  CO p-v diagram, fine-structure lines may be promising alternatives to be tracers for such activity. This can be seen in the p-v diagrams of [CII]  $158\mu\text{m}$  and [OI]  $63\mu\text{m}$ ; these two lines give the most prominent signature of cloud-cloud collision as the “bridge effect” can now be seen. As we discussed above, the emission of both [CII]  $158\mu\text{m}$  and [OI]  $63\mu\text{m}$  lines originate from the outer envelope of both GMCs and their surrounding ISM gas, which corresponds to gas that has not yet suffered any collision and still carries the information of the relative velocity of GMCs prior to collision. They can thus be used in order to identify and/or clarify the collision process in systems whose low- $J$  CO lines may provide limited information.

The bottom row of Fig. 2 shows the high velocity gas traced by each line. These maps correspond to the  $t = 4\text{ Myr}$  snapshots. The grayscale shows the total intensity,  $W$ , of each line. Red contours correspond to redshifted gas with velocities  $v > +5\text{ km s}^{-1}$  and blue contours to blueshifted gas with velocities  $v < -5\text{ km s}^{-1}$ . In both cases, the contours correspond to the intensity of the line. We do not include velocities in the range  $-5 < v < +5\text{ km s}^{-1}$  as we want to isolate the bulk motion of the gas due to collision and the mutual interaction of the GMCs rather than additionally mapping the width reached due to turbulence. The Doppler shifts of both the CO  $J = 1 - 0$  transition and the [CII] (1-0) line reveal the collision at  $z \sim -10\text{ pc}$  and  $y \sim +10\text{ pc}$  corresponding to the region with the highest density. However, the fine-structure lines of [CII]  $158\mu\text{m}$  and [OI]  $63\mu\text{m}$  reveal the bulk movement of GMCs and are thus good indicators of cloud-cloud collisions.

Emission from the ambient rarefied medium becomes considerable when studying the above fine-structure lines in these simulations. To clarify the role and the contribution of this gas in our results, we calculate the p-v diagram of [CII]  $158\mu\text{m}$  and [OI]  $63\mu\text{m}$  lines emitted by densities  $n_{\text{H}} > 20\text{ cm}^{-3}$  at  $t = 2\text{ Myr}$ . For densities below  $20\text{ cm}^{-3}$ , we consider negligible contribution in optical depth. This ensures that the

p-v diagram will contain information from both GMCs only. This is shown in the upper row of Fig. 3, whereas the bottom row shows additionally the contribution from the ambient gas. Comparing the p-v diagrams in the first column, we see that although the “bridge-effect” is seen in both cases, the antenna temperature is stronger in the upper panel (“GMC only”). This is because the emission of [CII] originates primarily from the lower density gas in both GMCs rather than from the ambient gas, the latter of which adds an optical depth along the line-of-sight which weakly reduces that emission. On the other hand, the emission originating from the GMC for the [OI]  $63\mu\text{m}$  line is much lower than that from the ambient gas (the antenna temperature is  $\sim 10$  times weaker). In the lower panel, the three well-defined stripes of antenna temperature correspond to the contribution of the ambient medium. The upper and lower stripes are due to the red-shifted and blue-shifted component respectively (moving away and towards the observer at a constant speed of  $v_{\text{rel}} \pm 5\text{ km s}^{-1}$ ).

#### 4.2. Non-colliding case

Figure 4 shows the emission maps, p-v diagrams and high velocity gas maps for the non-colliding case at  $t = 4\text{ Myr}$ . The emission maps in all four different lines are qualitatively similar to the colliding case at this dynamical time (see Fig. 2 for comparison). However, the intensities of CO  $J = 1 - 0$  and [CII] (1-0) are now lower since the system does not reach the necessary high densities and therefore the high column densities as previously. On the other hand, the emission maps of [CII] and [OI] lines do not significantly differ from the colliding case. The lower column densities reached in this simulation do not shield the  $158\mu\text{m}$  line and it thus remains brighter than the corresponding one of Fig. 2.

The velocity widths of the p-v diagrams in Fig. 4 are all within the  $-5 \lesssim v_{\text{los}} \lesssim +5\text{ km s}^{-1}$  range which results from the turbulent internal motion of the gas in both GMCs. The interesting feature, however, is that the intensity-weighted velocity gradient for the CO  $J = 1 - 0$  and [CII] (1-0) lines is decreasing along the position axis in the p-v diagrams. This

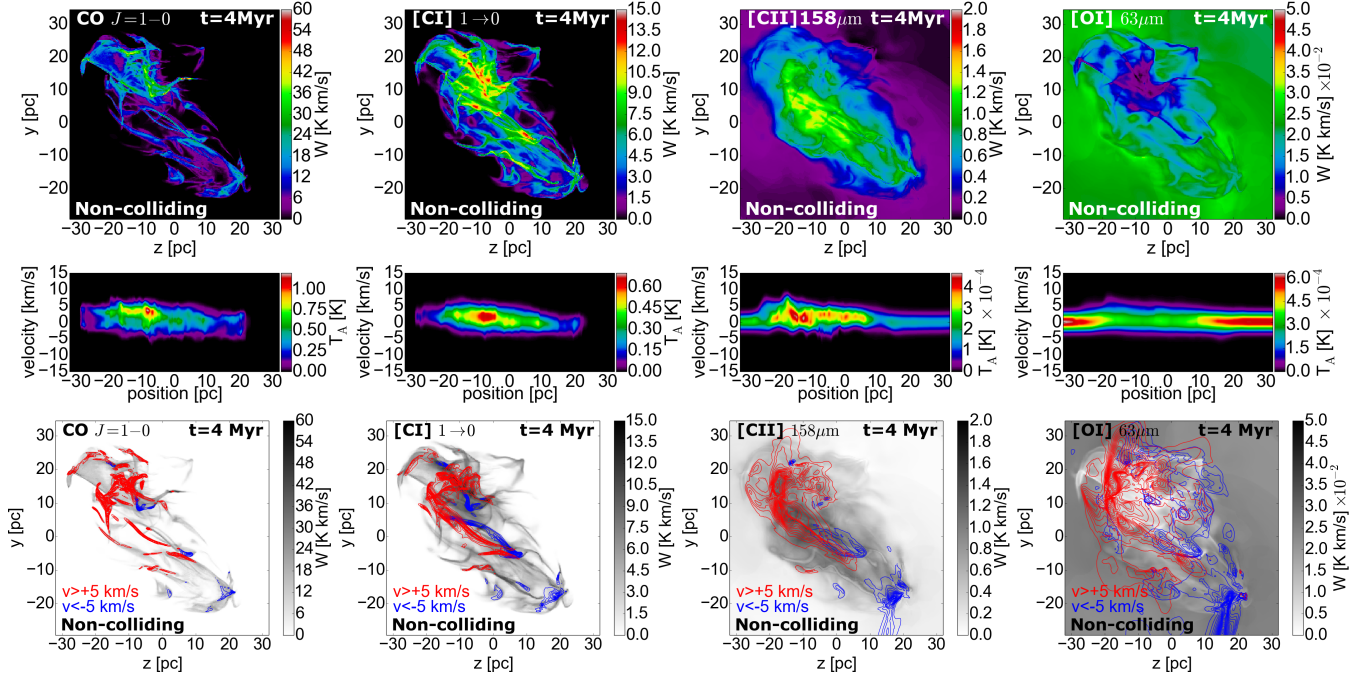


**Figure 4.** As in Fig. 2 for the non-colliding case. Here we plot the emission maps, p-v diagrams and the high velocity gas for  $t = 4$  Myr only. From the p-v diagrams it can be seen that in all cases we find a width of  $< 8 \text{ km s}^{-1}$  corresponding to the turbulent velocity dispersion due to the internal gas motions in each GMC. The gravitational forces acting on both clouds result in their mutual attraction. This can be observed in the high velocity gas maps in which the upper-left part is redshifted and the bottom-right is blueshifted. However, in none of the cases do we observe an interaction pointing to a collision, such as seen in Fig. 2.

is due to the mutual gravitational forces attracting both GMCs and which are best seen in all high velocity gas maps in the bottom row of the figure. In these maps it can be seen that the red- ( $v_{\text{los}} > +5 \text{ km s}^{-1}$ ) and blue- ( $v_{\text{los}} < -5 \text{ km s}^{-1}$ ) shifted components do not overlap as shown in the bottom row of Fig. 2, different from the cloud-cloud collision case.

### 5. DISCUSSION

Being able to identify collisions between GMCs is potentially important for our understanding of the global star formation process in galaxies. Theoretical models show that the broad “bridge-effect” (§3) in p-v diagrams is an excellent indicator of such activity. Observational surveys have revealed several cases of on-going cloud-cloud collision events. However, both models and observations primarily discuss such signatures in p-v diagrams of low- $J$  CO transition lines. Our work complements these results by first analyzing the results of realistic MHD simulations of colliding, turbulent, multiphase GMCs, and then exploring how fine-structure lines compare with CO  $J = 1 - 0$ . This work differs from the studies of Haworth et al. (2015a,b) by considering a more realistic physical model that includes magnetic fields and PDR-based heating/cooling, a concomitant improved treatment for the abundance and level populations of CO (whereas they assumed a constant abundance of  $[\text{CO}]/[\text{H}] = 8 \times 10^{-5}$  throughout their clouds), and a calculation of the radiative transfer of the fine-structure lines.

Our main finding is that the lines of [CI] (1-0), [CII]  $158 \mu\text{m}$  and [OI]  $^3\text{P}_1 \rightarrow ^3\text{P}_0$  transition at  $63 \mu\text{m}$ , are promising alternative ways for identifying cloud-cloud collisions via the “bridge-effect.” As the collision progresses and the denser parts of the clouds merge, the “bridge-effect” diminishes and low- $J$  CO lines then hardly show any signature of the collision. On the other hand, the lifetime of the broad bridge in fine-structure lines is predicted to be longer since these lines are emitted from the more rarefied parts of GMCs which are

primarily located at their outer envelopes that have not yet undergone collision.

The models considered here are based on an idealized situation in which there is no local stellar feedback. However, cloud-cloud collisions are potential sites for triggered star formation (Fukui et al. 2015, 2017a,b; Torii et al. 2015, 2017) leading to the birth of massive,  $\gtrsim 10 M_{\odot}$  stars (Takahira et al. 2014; Balfour et al. 2015). Thus the signatures of the PDRs from such localized stellar feedback (see, e.g., for examples of models of HII region feedback Dale et al. 2012; Walch et al. 2015; Haworth et al. 2015a) may confuse those from the bulk original GMC material, externally irradiated. Such contributions also need to be accounted for when interpreting observational data that includes localized PDRs. Thus the models presented here are most useful for isolating the “pure” signature of the GMC-GMC collision, which may be most easily compared to observations of GMCs in relatively early stages of collision and star formation.

Another simplification of our treatment is that in the post-processing of the MHD simulations, the gas is assumed to be in local thermodynamic equilibrium and additional transient heating effects from shocks are ignored. A future paper in this series will explore the importance of such effects.

As mentioned in §4, the collision occurs along the line-of-sight of the observer, which is the most idealized scenario for observations. As studied by Haworth et al. (2015a), the “bridge-effect” is relatively sensitive to the point of view of the observer and it diminishes as one departs from the face-on point of view. In Fig. 5 we show the emission map and p-v diagram of the [CII] line at  $t = 4$  Myr when the observation is made perpendicular to the direction of the collision. In this case, any signature of the cloud-cloud collision is minimized, and the velocity width now is in principle connected with the internal turbulence of the gas. However, the emission map shows a characteristic feature of a rectangular shape spanning

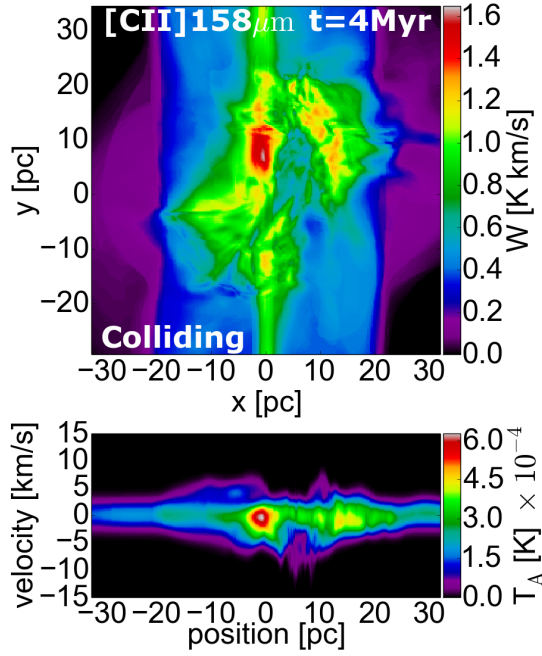


**Figure 5.** Emission map and p-v diagram of the colliding case in the [CII] 158  $\mu\text{m}$  line at  $t = 4$  Myr. The radiative transfer calculations have been performed along the  $z$ -direction which is perpendicular to the direction of the collision. The stripe at  $x \sim 0$  pc and along the  $y$ -direction in the emission map is due to the collision of the ambient medium. As expected, in the p-v diagram we do not observe any feature pointing to a collision event. Instead, the width in velocity space is due to the internal gas motions (i.e., internal turbulence) rather than the bulk motion of each GMC.

$\sim 40$  pc (from  $-20$  to  $+20$  pc) with a bright stripe at  $x \sim 0$  pc across the  $y$ -axis. This originates from the ambient ISM gas in which both GMCs are embedded. Still, in the typical case one expects some component of the collision axis to be along the line of sight and the purely perpendicular case will be a relatively unlikely occurrence.

## 6. CONCLUSIONS

In this paper we performed synthetic observations of  $^{12}\text{CO}$   $J = 1 - 0$ , [CI] (1-0), [CII] 158  $\mu\text{m}$  and [OI] 63  $\mu\text{m}$  in snapshots of MHD simulations carried out in Paper II of this series. The selected snapshots examine the colliding case of two GMCs, and the non-colliding case of two GMCs that overlap each other along the line-of-sight of the observer. With a simple radiative transfer tool, we calculated integrated intensity emission maps (including of high velocity components) and position-velocity diagrams for all the above four lines. We demonstrated that fine-structure lines, and in particular [CII] 158  $\mu\text{m}$ , may be a promising alternative tracer of cloud-cloud collisions, separate from the more commonly discussed CO lines. This finding holds even when the collision has been evolved so that the denser regions have merged and that low- $J$  CO lines are no longer good tracers of the collision. Our results are summarized as follows:

- The CO  $J = 1 - 0$  emission is overall stronger in the colliding than in the non-colliding case and in particular at the region where the collision occurs (peak of the total H-nucleus column density). The p-v diagram in the colliding case does not show a clear signature reminiscent to the “bridge-effect” mainly because the collision has been evolved to an extent that the CO-rich gas has been mixed up and such a signature is diminished. On the other hand, the integrated intensity maps of blue-

and redshifted high velocity gas do show in a clear way whether or not the two GMCs along the line-of-sight are colliding.

- The [CI] (1-0) line corresponding to a wavelength of 609  $\mu\text{m}$  is found to be emitted from the more diffuse gas of both GMCs. Although it peaks in the position where the two GMCs collide, it does not fluctuate as much as the CO  $J = 1 - 0$  line and its intensity does not significantly differ in the non-colliding case. The “bridge-effect” is observable in the p-v diagram at  $t = 2$  Myr in the colliding case, however at  $t = 4$  Myr it has disappeared. As with the CO  $J = 1 - 0$  line, the high velocity maps are able to indicate the collision event at all times.
- The fine-structure [CII] 158  $\mu\text{m}$  shows the most clear signature of the “bridge-effect” in the p-v diagrams of the colliding case. This line is emitted from the outermost parts of both GMCs with contributions from the ambient ISM gas (since it is rarefied and interacts with the isotropic FUV radiation). Its emission decreases as the collision progresses, since the density increases shielding the FUV radiation. The blue- and redshifted high velocity gas overlaps almost everywhere in the colliding case. In the non-colliding case, these maps show a mutual interaction without this leading to collision.
- The [OI]  $^3\text{P}_1 \rightarrow ^3\text{P}_0$  transition corresponding to 63  $\mu\text{m}$  follows the same behaviour as the [CII] line does. It is however much weaker with significant contributions from the ambient ISM gas. In places with total H-nucleus column densities of  $\gtrsim 5 \times 10^{22} \text{ cm}^{-2}$ , its intensity is almost negligible. Like [CII], the high velocity gas maps are able to indicate cloud-cloud collision events.

All p-v diagrams in the non-colliding case show a velocity width corresponding to internal turbulent gas motions, i.e., at approximately virialized velocities. Furthermore, in all the above cases, we have assumed that the collision occurs along the line-of-sight of the observer. If at an angle, any possible signature will be diminished and completely eliminated in the rare case that the collision occurs perpendicular to the observer.

We thank Thomas Haworth for useful discussions. KT thanks Kazuhito Motogi and Taishi Nakamoto. BW is thankful for support from the Japan Society for the Promotion of Science Postdoctoral Fellowship.

## REFERENCES

- Balfour, S. K., Whitworth, A. P., Hubber, D. A., & Jaffa, S. E. 2015, MNRAS, 453, 2471
- Bisbas, T. G., Bell, T. A., Viti, S., Yates, J., & Barlow, M. J. 2012, MNRAS, 427, 2100
- Bisbas, T. G., Bell, T. A., Viti, S., et al. 2014, MNRAS, 443, 111
- Bisbas, T. G., Papadopoulos, P. P., & Viti, S. 2015, ApJ, 803, 37
- Bisbas, T. G., van Dishoeck, E. F., Papadopoulos, P. P., et al. 2017, ApJ, 839, 90
- Bryan, G. L., Norman, M. L., O’Shea, B. W., et al. 2014, ApJS, 211, 19
- Christie, D., Wu, B., & Tan, J. C., 2017, *submitted*
- Dale, J. E., Ercolano, B., & Bonnell, I. A. 2012, MNRAS, 424, 377
- Dobbs, C. L., Pringle, J. E., & Duarte-Cabral, A. 2015, MNRAS, 446, 3608
- Duarte-Cabral, A., Fuller, G. A., Peretto, N., et al. 2010, A&A, 519, A27

Duarte-Cabral, A., Dobbs, C. L., Peretto, N., & Fuller, G. A. 2011, *A&A*, 528, A50  
 Fukui, Y., Torii, K., Hattori, Y., et al. 2017a, arXiv:1701.04669  
 Fukui, Y., Tsuge, K., Sano, H., et al. 2017b, *PASJ*, 69, L5  
 Fukui, Y., Harada, R., Tokuda, K., et al. 2015, *ApJ*, 807, L4  
 Fukui, Y., Ohama, A., Hanaoka, N., et al. 2014, *ApJ*, 780, 36  
 Gammie, C. F., Ostriker, J. P., & Jog, C. J. 1991, *ApJ*, 378, 565  
 Glover, S. C. O., & Clark, P. C. 2016, *MNRAS*, 456, 3596  
 Habing, H. J. 1968, *Bull. Astron. Inst. Netherlands*, 19, 421  
 Haworth, T. J., Tasker, E. J., Fukui, Y., et al. 2015a, *MNRAS*, 450, 10  
 Haworth, T. J., Shima, K., Tasker, E. J., et al. 2015b, *MNRAS*, 454, 1634  
 Higuchi, A. E., Kurono, Y., Saito, M., & Kawabe, R. 2010, *ApJ*, 719, 1813  
 Inoue, T., & Fukui, Y. 2013, *ApJ*, 774, L31  
 Jin, K., Salim, D. M., Federrath, C., et al. 2017, *MNRAS*, 469, 383  
 Li, Q., Tan, J. C., Christie, D., Bisbas, T. G., & Wu, B. 2017, arXiv:1706.03764  
 McElroy, D., Walsh, C., Markwick, A. J., et al. 2013, *A&A*, 550, A36  
 Nakamura, F., Miura, T., Kitamura, Y., et al. 2012, *ApJ*, 746, 25  
 Offner, S. S. R., Bisbas, T. G., Bell, T. A., & Viti, S. 2014, *MNRAS*, 440, L81

Papadopoulos, P. P., Thi, W.-F., & Viti, S. 2004, *MNRAS*, 351, 147  
 Scoville, N. Z., Sanders, D. B., & Clemens, D. P. 1986, *ApJ*, 310, L77  
 Suwannajak, C., Tan, J. C., & Leroy, A. K. 2014, *ApJ*, 787, 68  
 Takahira, K., Tasker, E. J., & Habe, A. 2014, *ApJ*, 792, 63  
 Tan, J. C. 2000, *ApJ*, 536, 173  
 Tan, J. C. 2010, *ApJ*, 710, L88  
 Tan, J. C., Kong, S., Butler, M. J., Caselli, P., & Fontani, F. 2013, *ApJ*, 779, 96  
 Tasker, E. J., & Tan, J. C. 2009, *ApJ*, 700, 358  
 Torii, K., Hattori, Y., Hasegawa, K., et al. 2017, *ApJ*, 835, 142  
 Torii, K., Hasegawa, K., Hattori, Y., et al. 2015, *ApJ*, 806, 7  
 Torii, K., Enokiya, R., Sano, H., et al. 2011, *ApJ*, 738, 46  
 Walch, S., Whitworth, A. P., Bisbas, T. G., Hubber, D. A., & Wünsch, R. 2015, *MNRAS*, 452, 2794  
 Wu, B., Van Loo, S., Tan, J. C., & Bruderer, S. 2015, *ApJ*, 811, 56  
 Wu, B., Tan, J. C., Nakamura, F., et al. 2017a, *ApJ*, 835, 137  
 Wu, B., Tan, J. C., Christie, D., et al. 2017b, *ApJ*, 841, 88

## APPENDIX

### RADIATIVE TRANSFER ALGORITHM

We describe here the algorithm of radiative transfer calculations we develop which was used in all synthetic maps in this work (see also §2.3). We begin by solving the radiative transfer equation along the line-of-sight element  $dz$ :

$$\frac{dI_\nu}{dz} = -\alpha_\nu I_\nu + \alpha_\nu S_\nu, \quad (\text{A1})$$

where  $I_\nu$  is the intensity of the line,  $\alpha_\nu$  the absorption coefficient, and  $S_\nu$  is the source function at frequency  $\nu$ . The source function and the absorption coefficient for a transition of  $i \rightarrow j$  are

$$S_\nu = \frac{2h\nu_0^3}{c^2} \frac{n_i g_j}{n_j g_i - n_i g_j}, \quad (\text{A2})$$

$$\alpha_\nu = \frac{c^2 n_i A_{ij}}{8\pi\nu_0^2} \left( \frac{n_j g_i}{n_i g_j} - 1 \right) \phi_\nu, \quad (\text{A3})$$

where  $\nu_0$  is the frequency of the line center,  $A_{ij}$  is the Einstein A coefficient,  $n_i, n_j$  are the level populations, and  $g_u, g_l$  are the statistical weights of levels  $i, j$ , and  $\phi_\nu$  is the line profile. The level populations are obtained from our photodissociation region calculations using 3D-PDR (see §2.2 Bisbas et al. 2012). We assumed a Maxwellian distribution of velocities due to the thermal and the turbulent gas motion. The line profile takes, therefore, the form

$$\phi_\nu = \frac{1}{\sqrt{2\pi\sigma_\nu^2}} \exp \left\{ -\frac{[(1 + v_{\text{los}}/c)\nu - \nu_0]^2}{2\sigma_\nu^2} \right\}, \quad (\text{A4})$$

where  $v_{\text{los}}$  is the gas velocity along the line-of-sight (positive for red-shift and negative for blue-shift), and  $\sigma_\nu$  is the dispersion defined as

$$\sigma_\nu = \frac{\nu_0}{c} \sqrt{\frac{k_B T_{\text{gas}}}{m_{\text{mol}}} + \frac{v_{\text{turb}}^2}{2}}, \quad (\text{A5})$$

where  $T_{\text{gas}}$  is the gas temperature,  $m_{\text{mol}}$  is the mass of the molecule/ion emitting the line, and  $v_{\text{turb}}$  is the a root mean-square measure of turbulent velocities (set to be  $v_{\text{turb}} = 5 \text{ km s}^{-1}$  throughout the radiative transfer calculations presented here).

The formal solution of radiative transfer equation (Eqn. A1) is given by

$$I_\nu(z) = I_\nu(0)e^{\tau_\nu(z)} + \int_0^{\tau_\nu(z)} S_\nu(z')e^{\tau'_\nu - \tau_\nu(z)} d\tau'_\nu, \quad (\text{A6})$$

where  $\tau_\nu = \int_0^z \alpha_\nu(z')dz'$  is the optical depth. To solve the radiative transfer numerically, the source function and the absorption coefficient are assumed to be linear between each grid  $[z_p, z_{p+1}]$ . Then, the differential solution can be obtained as

$$I_{\nu,p+1} = I_{\nu,p}e^{-\Delta\tau_\nu} + S_{\nu,p} \left( \frac{1 - e^{-\Delta\tau_\nu}}{\Delta\tau_\nu} - e^{\Delta\tau_\nu} \right) + S_{\nu,p+1} \left( 1 - \frac{1 - e^{-\Delta\tau_\nu}}{\Delta\tau_\nu} \right), \quad (\text{A7})$$

$$\Delta\tau_\nu = \frac{\alpha_{\nu,p} + \alpha_{\nu,p+1}}{2} dz, \quad (\text{A8})$$



where the subscripts of  $p$  and  $p + 1$  denote the position of variables. This form of the solution can reproduce the physical consequences at both optically thin and thick limits:

$$I_{\nu,p+1} = \begin{cases} I_{\nu,p}(1 - \Delta\tau_\nu) + \frac{B_{\nu,p} + B_{\nu,p+1}}{2} \Delta\tau_\nu & (\Delta\tau_\nu \rightarrow 0), \\ B_{\nu,p+1} & (\Delta\tau_\nu \rightarrow \infty). \end{cases} \quad (\text{A9})$$

For boundary conditions, we adopt the intensity of the Cosmic Microwave Background Radiation of 2.7 K, i.e.  $I_\nu(z = 0) = B_\nu(2.7K)$  where  $B_\nu$  is the Planck function. The line profile is obtained by solving Eqn. A6 for the frequency range  $[\nu_0 - \Delta\nu/2, \nu_0 + \Delta\nu/2]$ , where  $\Delta\nu \ll \nu_0$  is the band width.